Achievement of Excellent Thermoelectric Properties in Cu-Se-S Compounds via In-Situ Phase Separation

Yi-Xin Zhang,[a] Yun-Qiao Tang,[a] Zheng Ma,[b] Ming-Yu Hu,[a,c] Jing Feng,[a] and Zhen-Hua Ge*[a]*

[a] Faculty of Materials Science and Engineering, Kunming University of Science and Technology, Kunming, 650093, China. E-mail: Z.-H. Ge (zge@kust.edu.cn)

[b] Ernst Ruska-Centre for Microscopy and Spectroscopy with Electrons and Peter Grünberg Institute, Forschungszentrum Jülich, 52425 Jülich, Germany.

[c] School of Chemical Biology and Biotechnology, Shenzhen Graduate School, Peking University, Shenzhen 518055, China

ABSTRACT: In this study, $Cu_2Se_{1-x}S_x$ (x=0.1, 0.3, and 0.5) alloy powders were prepared by the hydrothermal synthesis (HS) method. In the subsequent sintering process, the spontaneous in situ phase separation process of the sample forms a two-phase hybrid structure. The generated Cu_2S precipitates in the Cu_2Se matrix noticeably enhance phonon scattering, beneficial for low thermal conductivity without significantly affecting the electrical transport performance. Ultimately, the optimized thermoelectric performance was obtained in $Cu_2Se_{0.9}S_{0.1}$, reaching a peak zT value of 1.43 at 773 K, the optimum value among the Cu-Se-S systems at this temperature.

KEYWORDS: $Cu_2Se_{1-x}S_x$, hydrothermal synthesis, phase separation, thermoelectric properties

INTRODUCTION

Thermoelectric (TE) energy conversion technology has attracted widespread focus as a strategy of energy issues for more efficient utilization of energy resources and primary power generation.[1-8] Generally, thermoelectric materials and their devices can directly convert heat derived from industrial waste heat, nuclear fuel, or even biothermal energy to electricity.[9-12] In the TE materials research field, one of the principal goals is to maximize the dimensionless thermoelectric figure of merit (zT):

$$zT = \frac{\alpha^2 \sigma}{\kappa} T \quad (1)$$

where α is the Seebeck coefficient (i.e., thermopower or voltage divided by the temperature gradient), σ is the electrical conductivity, κ is the thermal conductivity, and T is the absolute temperature at which the materials were applied.[13,14] The challenge is to obtain a TE material with an excellent zT value to satisfy the usage efficiency, since α, σ, and κ in one material is highly dependent on the carrier concentration, resulting in a strong coupling effect to obstruct the simultaneous optimization of these parameters.[15-18] In this scenario, this work focuses on searching for a feasible approach to dramatically decrease the thermal conductivity of materials but slightly affect the electrical transport performance, which is very valuable.

Traditional high-performance TE materials, such as Bi_2Te_3,[19,20] PbTe[21,22], and Si-Ge alloys, encounter the common issues of costly and toxic properties, although some of them have already been commercialized. With the rise of sustainable development and environmental protection concepts, researchers are increasingly interested in developing a new generation of efficient thermoelectric materials with low cost, environmental friendliness, and earth-abundant elements. In addition, the "Phonon-Liquid Electron-Crystal" (PLEC) concept[23] has been proposed to understand Cu/Ag-based superionic conductors, such as $Cu_{2-x}Se$[24] and $Cu_{2-x}S$,[25] containing liquid-like ions in the specific

temperature range. Thus, these materials show great potential in thermoelectric applications due to their extremely low thermal conductivity and superior electric performance.

Copper chalcogenides $Cu_{2-x}X$ (X=S, Se, or Te) have complex crystal structures. For instance, $Cu_{2-x}S$ ($0 < x < 1$) varies from Cu-rich Cu_2S to Cu-poor CuS,[26] and the intermediate phases, including $Cu_{1.96}S$, Cu_9S_5, and Cu_7S_4, were also reported by Zhao et al.[27] $Cu_{2-x}X$ is a normal solid compound with ordered copper ions in the crystal lattice at room temperature.[28] As the temperature rises, the copper chalcogenides experience phase transitions and change to the liquid-like compounds, and the transition temperature depends on the exact chemical compositions. $Cu_{2-x}X$ usually possesses an anti-fluorite cubic structure at high temperatures.[29-30] Thus, the compounds may possess a similar crystal structure to form a complete/partial solid solution. Surprisingly, a solid solution with a mosaic crystal microstructure could be obtained in Cu_2S/Cu_2Te, although there is a large atomic size difference between S and Te.[31] Therefore, Cu_2Se and Cu_2S more easily form solid solutions,[32-36] the effects of doping Se in Cu_2S and doping S in Cu_2Se have been studied, which reveal that the Cu-Se-S solid solution could be achieved by the solid state reaction or the mechanical alloying, and the thermoelectric performance could be enhanced compared to that of the pure Cu_2S or Cu_2Se materials. Besides, introducing Cu deficiencies in $Cu_{2-x}Se_{0.5}S_{0.5}$ or compositing $Cu_{2-x}Se$ with Cu_2S have been proved to be the effective strategies to optimize the thermoelectric properties.

In our previous work, an ultrahigh conductivity (σ) up to 2490 Scm^{-1} was achieved in the binary compound $Cu_{2-x}S$ synthesized by the hydrothermal synthesis (HS) method.[37] Cu_2Se samples with intrinsically low thermal conductivity were reported by Liu et al.[23] Therefore, the solid solutions of $Cu_2Se_{1-x}S_x$ may reach an excellent zT value. In this work, the $Cu_2Se_{1-x}S_x$ (x=0.1, 0.3, and 0.5) alloy powders were fabricated by HS method. In the subsequent sintering process, the spontaneous in situ

phase separation of the sample formed a two-phase hybrid structure and caused the nanosized precipitates on the substrate, greatly enhancing the scattering of phonons and decreasing the thermal conductivity with a slight change in the electrical transport performance. The comparison of the dimensionless figure of merit and average zT value during 323 K to 773 K for Cu_2Se based materials are shown in Figure 1. The special semi coherent boundaries between Cu_2S precipitates and Cu_2Se matrix contribute to good electrical transport properties, and very low thermal conductivity, resulting in a superior zT peak value of 1.43 at 773 K for $CuSe_{0.9}S_{0.1}$ sample.

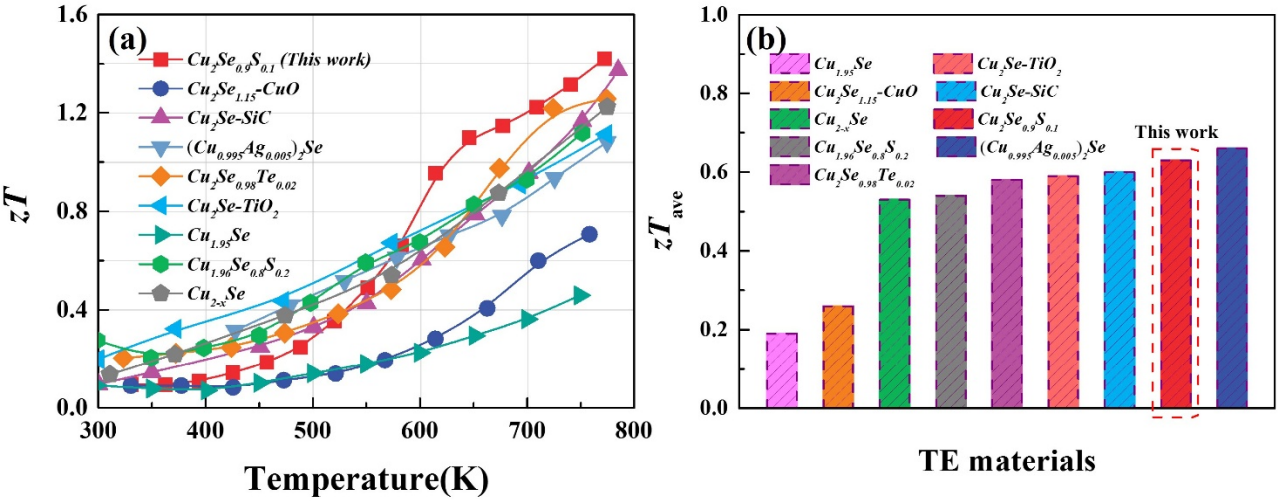

Figure 1. (a) Temperature dependence of zT values compared with other copper sulfides and (b) The average zT value of $Cu_2Se_{0.9}S_{0.1}$ in this work and of other Cu_2Se-based TE materials during 323 K to 773 K.[36-43]

EXPERIMENTAL SECTION

The CuO (99.5%), Se (99.9%), and S (99.99%) powders were purchased from Aladdin and employed as the raw materials. Commercial high-purity liquors of ethylene diamine (EDA) were used as the chelating agent and solvent, and hydrazine hydrate was the reducing agent. In the synthetic procedure, 0.01 mol CuO, 0.0025 mol Se and S were added to 40 ml EDA, and the solution was stirred for 30 min. Afterward, 35 ml ethylene glycol was added into the solution and stirred for 10 min. The

resulting mixture solution was then transferred into a Teflon-lined stainless-steel autoclave (100 mL capacity) and reacted at 473 K for 12 h. The final solid product was washed with DI water and ethanol three times and dried under vacuum at 333 K for 12 h.

The synthesized powders were ground manually in a glove box and sintered at 773 K for 5 min (heating rate of 100 K/min) in a Φ15 mm graphite mold under axial compressive stress of 40 MPa in vacuum by using an SPS system (SPS-632 LX, Fuji electric, Aichi-ken, Japan). The SPSed specimens were cut and ground into disk-shaped specimens with dimensions of Φ6 mm × 2 mm and bars of 3 mm × 3 mm × 12 mm for thermal diffusivity and electrical resistivity measurements, respectively.

X-ray diffraction (XRD) patterns of powders and bulk specimens were recorded on a Miniflex600 operating at 40 kV and 15 mA using monochromatic Cu Kα radiation (λ=1.541 Å, step size=0.02°, 10° min-1 from 20 to 70). Full profile Rietveld refinements are carried out for $Cu_2Se_{1-x}S_x$ specimens using the program MAUD. Field-emission scanning electron microscopy (FESEM, SUPRA 55, Carl Zeiss, Oberkochen, Germany) was utilized to observe the powder microstructure and the fractured topography of the bulk specimens. Transmission electron microscopy (TEM, Phililp Tecnai F20, Dutch) was used to analyze the microstructure of the powder and bulk samples. Energy dispersive spectrometry (EDS) was performed to determine the actual chemical compositions. Electron probe microanalysis with wavelength dispersive spectrometry (EPMA, JEOL, JXA-8230, Japan) was used to determine the chemical distribution and composition of bulk samples.

The Seebeck coefficient and electrical resistivity were tested from 323 to 773 K in a helium atmosphere using a Seebeck coefficient/electrical resistance measuring system (ZEM-3, Ulvac-Riko, Japan). The density (d) of the bulk specimens was measured by the Archimedes method. Additionally, the thermal conductivity of the samples was calculated by the relationship $\kappa=DCpd$ from the thermal

diffusivity D measured by the laser flash method (LFA457, NETZSCH, Germany) and the specific heat C_p was calculated by Neumann-Kopp rule. The error bars have been added in the experimental data. The absolute error of the Seebeck coefficient, electrical resistivity, and thermal conductivity can be assumed to be 3%~4%, then the error bar of zT would be 15%~20%.

RESULTS AND DISCUSSION

X-ray diffraction is utilized to detect the phase structure of the fabricated $Cu_2Se_{1-x}S_x$ (x=0.1, 0.3, 0.5) powders at room temperature. The solved crystal structure of $Cu_2Se_{1-x}S_x$ in the high temperature is exhibited in Figure 2a, among which the Se/S atoms form a rigid framework, and the Cu ions are concentrated at the tetrahedral interstices 8c (1/4, 1/4, 1/4) sites. The lattice contracts as the S content increases, indicating the Se sites are fully occupied by half Se and S. All the diffraction peaks of $Cu_2Se_{1-x}S_x$ powders displayed in Figure 2b can be clearly indexed to the standard card (JSPDS no. 06-0680), indicative of the successfully obtained $Cu_2Se_{1-x}S_x$ powders composed of $Cu_{2-x}Se$ and tiny content of Cu_2S. Furthermore, the diffraction peaks of the $Cu_2Se_{0.5}S_{0.5}$ powder noticeably shift to a higher angle than the other two powders, and the shrinkage of the matrix lattice might be due to the Se^{2-} (1.98 Å) sites occupied by S^{2-} (1.84 Å). Additionally, the widened diffraction peak of the $Cu_2Se_{0.5}S_{0.5}$ sample might be ascribed to the refined grains. The actual chemical compositions of the powder samples were determined by EDS, as shown in Figure S1, implying the successful preparation of $Cu_2Se_{0.9}S_{0.1}$, $Cu_2Se_{0.7}S_{0.3,}$ and $Cu_2Se_{0.5}S_{0.5}$ powders.

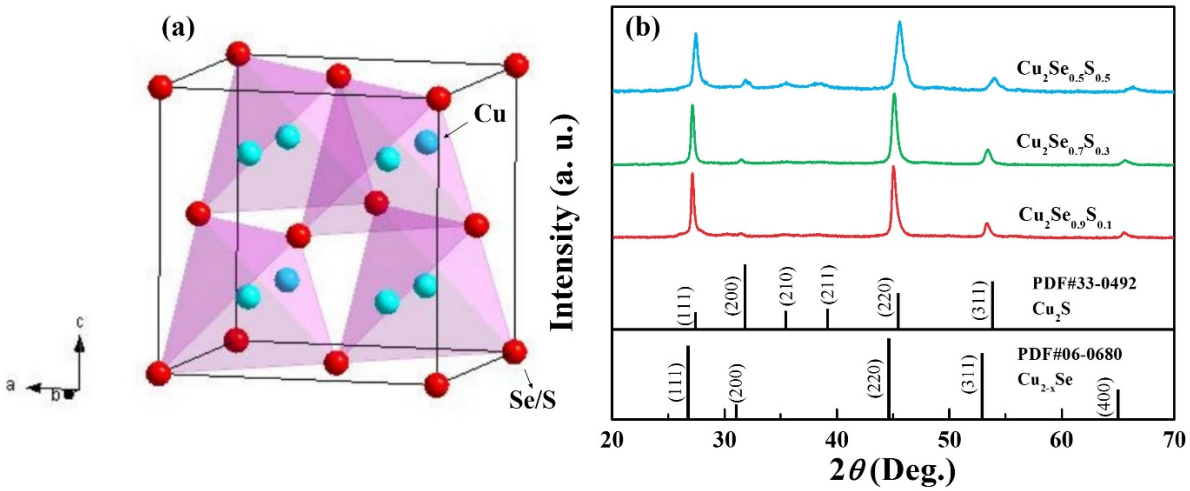

Figure 2. (a) Schematic diagram of the crystal structure (*F-43m*) of Cu-Se-S alloy obtained from single crystal structural solution at room temperature, the purple tetrahedron illustrates the disordered Cu sites. (b) XRD (Cu Kα) patterns for Cu-Se-S alloy powders prepared with different Se/S ratio.

The microstructures of the $Cu_2Se_{1-x}S_x$ (x=0.1, 0.3 and 0.5) alloy powders in scanning electron microscopy (SEM) and transmission electron microscopy (TEM) images are displayed in Figure 3 (Figure 3a-b, $Cu_2Se_{0.5}S_{0.5}$; Figure 3c-d, $Cu_2Se_{0.7}S_{0.3}$; Figure 3e-f, $Cu_2Se_{0.9}S_{0.1}$). It can be observed that the morphology of the $Cu_2Se_{1-x}S_x$ powders is a very thin hexagonal sheet with a diameter of 100 nm–1.5 μm. Nanosheets tend to arrange along one direction and change to thick sheets at high temperatures during the hydrothermal procedure.[44] The powder grains gradually refined as the S content increased, matching the XRD results. Herein, the introduction of S results in lattice distortion of Cu_2Se and increasing system complexity, which would affect the thermoelectric properties. Moreover, the lattice spacing of the (220) plane decreases from 0.2362 nm to 0.2031 nm with increasing S content, signifying lattice shrinkage in $Cu_2Se_{1-x}S_x$ by S doping. The Rietveld refinement patterns of Cu-Se-S powders are added in the Figure S2a-c, indicating the existing of Cu-Se-S solid solutions. Based on the refinement data, the lattice parameters for as-synthesized powder samples were calculated and added in the Figure S3 as well. Due to the smaller atomic size of S (1.04 Å) than that of Se (1.17 Å),

the introduction of sulfur results in the shrinkage of the lattice according to the Vegard's law (dash line), suggesting the solid solution of S in Cu_2Se matrix. Besides, the grains gradually refined with increasing sulfur content, leading the broadened diffraction peaks. The phenomenon of preferred orientation seems appears in the powder, which might be ascribe to the synthesized nano plates as shown in Figure 3 (FESEM and TEM images).

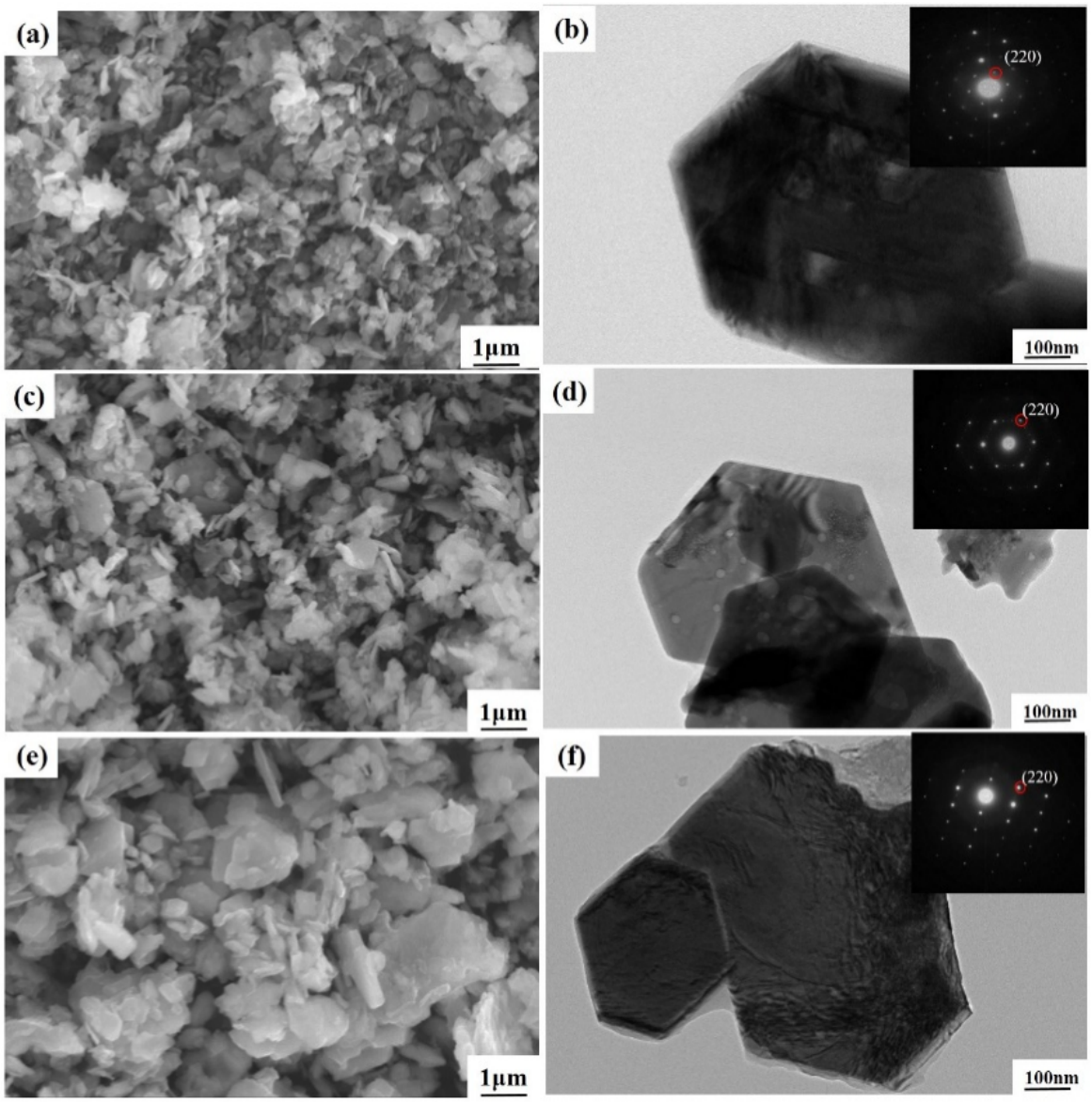

Figure 3. Microstructures of the $Cu_2Se_{1-x}S_x$ (x=0.1, 0.3 and 0.5) alloy powders. Field emission scanning electron microscopy (FESEM) patterns of the (a) $Cu_2Se_{0.5}S_{0.5}$ powder; (c) $Cu_2Se_{0.7}S_{0.3}$ powder and (e) $Cu_2Se_{0.9}S_{0.1}$ powder. High-magnification transmission electron microscope (TEM)

image with the corresponding selected area electron diffraction (SAED) pattern for the (b) $Cu_2Se_{0.5}S_{0.5}$ powder; (d) $Cu_2Se_{0.7}S_{0.3}$ powder and (f) $Cu_2Se_{0.9}S_{0.1}$ powder.

As described above, a series of $Cu_2Se_{1-x}S_x$ powder specimens have been successfully fabricated through the solution method with tiny content of Cu_2S precipitates. Bulk X-ray diffraction (BXRD) patterns of $Cu_2Se_{1-x}S_x$ (x=0.1, 0.3, and 0.5) at room temperature were collected to study the phase structure of $Cu_2Se_{1-x}S_x$ bulk specimens sintered by SPS, shown in Figure 4a. The prominent diffraction peaks of $Cu_2Se_{1-x}S_x$ bulks can be indexed to the $Cu_{2-x}Se$ structure, which is similar to the powder results. The Cu_2S phase appears in all the specimens after the sintering process, and the intensity of the impurity Cu_2S peaks rise with increasing S content. The Rietveld refinement patterns of Cu-Se-S bulk specimens are added in the Figure S3d-f. The intensity of (101) plane is larger than that of the (100) plane in Cu_2S, whereas the diffraction peak around 25.8° is higher than that of the 28.5°. The unreasonable relative intensity between the diffraction peaks corresponds to the preferred orientation, and this phenomenon appear obviously with increasing S content, resulting from the increased content of introduced nano-sized Cu_2S precipitates with hexagonal phase. Besides, since that the position of the two planes of (311) from $Cu_{2-x}Se$ and (112) from Cu_2S are adjacent, some of diffraction peaks change to the asymmetric shape especially for the $Cu_2Se_{0.5}S_{0.5}$ bulk sample. The diffraction peaks shift to the higher angle due to the shrinkage of lattice caused by the occupied Se sites by the S. Electron probe microanalysis (EPMA) was performed on these three polished bulk samples to determine the relative content and distribution of the Cu_2S phase. The relative content and distribution of copper, selenium, and sulfur in the three elements of the $Cu_2Se_{0.9}S_{0.1}$ bulk sample are shown in Figure 4b. The SPS sintered bulk specimen possesses a relatively dense structure, only nano-scaled pores exist in the substrate. It is worth noting that sulfur is evenly distributed in the material, meaning that a large amount

of S still enters the lattice and occupies the Se sites. However, the excessive S might be enriched in the Se-based framework and partially deprive Cu to generate the Cu_2S phase. The EPMA mapping where sulfur is enriched and selenium is missing could be Cu_2S precipitation. A similar phenomenon could be observed in the $Cu_2Se_{0.5}S_{0.5}$ and $Cu_2Se_{0.7}S_{0.3}$ specimens (Figure S3a-b), while the content of nano-scaled pores and Cu_2S precipitates increased as the S content grew, and their size enlarged.

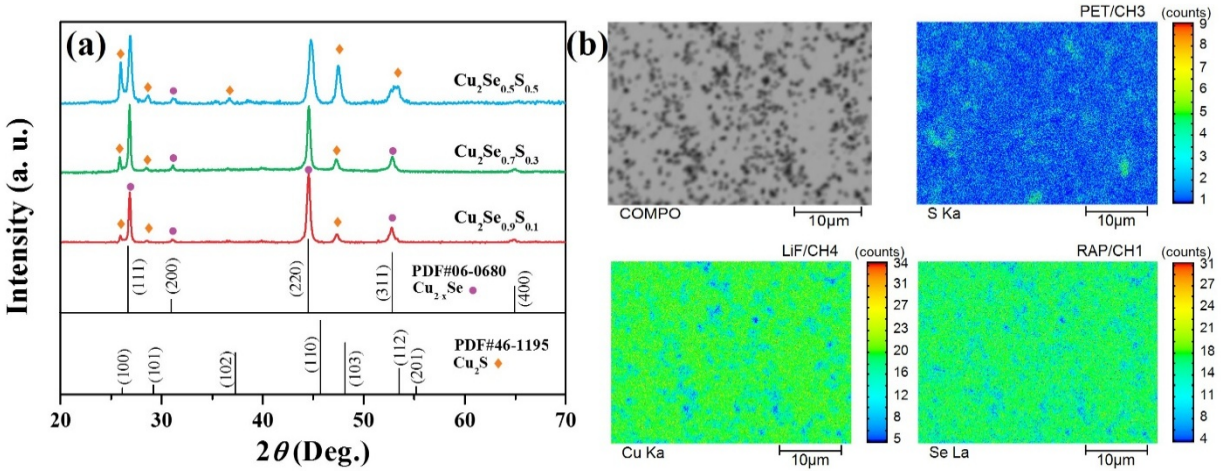

Figure 4. (a) XRD patterns for SPS treated Cu-Se-S bulk samples, (b) Electron probe microanalysis (EPMA) images of the $Cu_2Se_{0.9}S_{0.1}$ bulk specimen.

The representative area of the $Cu_2Se_{0.9}S_{0.1}$ bulk sample is presented in Figure 5a and Figure 5b, obtained by utilizing transmission electron microscopy (TEM) with different magnifications. Several precipitates with different shapes are dispersed on the substrate. Most irregular diamond-like precipitates are embedded in the matrix material, while some long strips of precipitates occasionally intersperse. Additionally, high-angle annular dark-field (HAADF) images and EDS mapping are displayed in Figure 5c and Figure 5d to discriminate the precipitate components, demonstrating that both diamond- and strip-like precipitates are Cu_2S. In addition, the legend in Figure 5c expresses the magnified TEM image with regular rectangular-shaped nanoparticles with precipitate and matrix interfaces along the [100] directions. The representative area where the diffraction fringes of the

substrate and the precipitates are evident is collected to confirm the structural relationship between Cu_2S and Cu_2Se, and the image with higher magnification is taken at the junction of the two phases, as shown in Figure 5e and Figure 5f. The interplanar spacing of the precipitated Cu_2S phase (=0.335 nm) is approximately half of the substrate Cu_2Se (=0.678 nm). The Cu_2S precipitates separate from the matrix material during the synthesis process, which could result from the free migration of Cu^+ in the Se^{2-}/S^{2-} framework during the sintering process. As discussed above, S occupied the Se sites during the powder synthesis process, and the Se framework composed of partial S was maintained even during the phase transition, similar to the rigid anion framework in other Cu-based liquid-like TE materials.[45,46] For the cations, Cu^+ could migrate freely in the Se/S framework when beyond the phase transition temperature and redistribute in the tetrahedral interstices, and then the Cu_2S phase was maintained in the Cu_2Se material at room temperature. Since the special crystallographic relationship between the (110) plane of Cu_2Se and the (100) plane of Cu_2S, approximately half of the interplanar spacing, a partial lattice framework of Cu_2S would be embedded into the Cu_2Se. In situ phase separation was also observed in AgCuTe-based materials,[47] but it was discovered in the Cu-Se-S system for the first time.

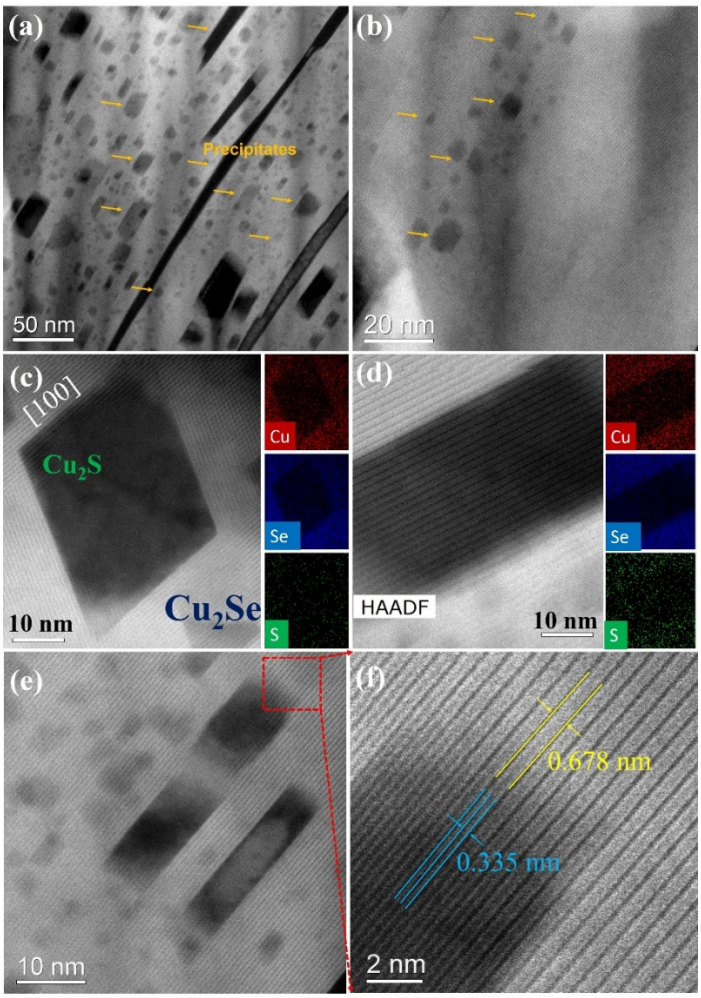

Figure 5. Microstructures of the "$Cu_2Se_{0.9}S_{0.1}$" bulk sample. (a) Low-magnification transmission electron microscope (TEM) image for the "$Cu_2Se_{0.9}S_{0.1}$" bulk. (b) High-magnification transmission electron microscope (TEM) image for the "$Cu_2Se_{0.9}S_{0.1}$" bulk. (c-f) High angle annular dark field (HAADF) image for the"$Cu_2Se_{0.9}S_{0.1}$" bulk and energy dispersive spectrometer (EDS) image for the Cu/Se/S elemental distribution.

Nanosized internal interfaces are introduced during phase separation, significantly affecting the electrical and thermal transport performance of Cu-Se-S alloys. In previous studies, nanostructured Cu_2S materials with high conductivity were successfully prepared by nanostructure adjustment under the premise of sacrificial intrinsic low thermal conductivity.[33] On this basis, the introduction of sulfur in Cu_2Se by the same method can improve its electrical transport properties. The variation in electrical

transport properties for $Cu_2Se_{1-x}S_x$ (x=0.1, 0.3, 0.5) in the temperature range from room temperature (RT) to 773 K is illustrated in Figure 6. The electrical conductivity (σ) curves are shown in Figure 6a, the fluctuation of the electrical conductivity of $Cu_2Se_{1-x}S_x$ specimens is caused by the phase transition. Cu_2S material undergoes a phase transition from monoclinic phase to the hexagonal phase around the 400 K, the Cu ions change to the disordered state and affect the hole migration beyond the 400 K, which thus cause the decreased carrier mobility and electrical conductivity with temperature. The content of Cu_2S precipitates in the $Cu_2Se_{0.7}S_{0.3}$ and $Cu_2Se_{0.5}S_{0.5}$ composites is higher than that of the $Cu_2Se_{0.9}S_{0.1}$ samples, hence the electrical conductivity of $Cu_2Se_{0.7}S_{0.3}$ and $Cu_2Se_{0.5}S_{0.5}$ express the different tendency with temperature from that of the $Cu_2Se_{0.9}S_{0.1}$ sample. Furthermore, the electrical conductivity dramatically increases after introducing S, mainly ascribed to the enhanced carrier concentration (see Figure 6c) obtained by doping S with higher electronegativity in Cu_2Se. The XRD results shown above reflect that the primary phase is $Cu_{2-x}Se$, and the Cu deficiency originates from the higher vacancy formation energy for Cu_2S. Zhao et al. proved that the Cu-S bond length (~2.29 Å) is shorter than the bond length in Cu-Se (~2.46 Å), suggesting the higher bond energy of Cu-S.[33] Therefore, the Cu atoms are easily to bond with the S atoms and cause the Cu deficiencies in the Cu_2Se. Consequently, the doping effect of Se by S and the generation of Cu deficiencies in Cu_2Se are beneficial for the enhancement of the hole carrier concentration in Cu-Se-S solid solution. However, the electrical conductivity was maintained after introducing excessive S (x>0.3) since that the carriers possess more opportunities to collide with the generated impurity which cause the carrier mobility reduction. Ultimately, the highest electrical conductivity of 531 Scm^{-1} is achieved for the $Cu_2Se_{0.5}S_{0.5}$ bulk sample at 773 K, noticeably higher than the Cu_2S and Cu_2Se samples.

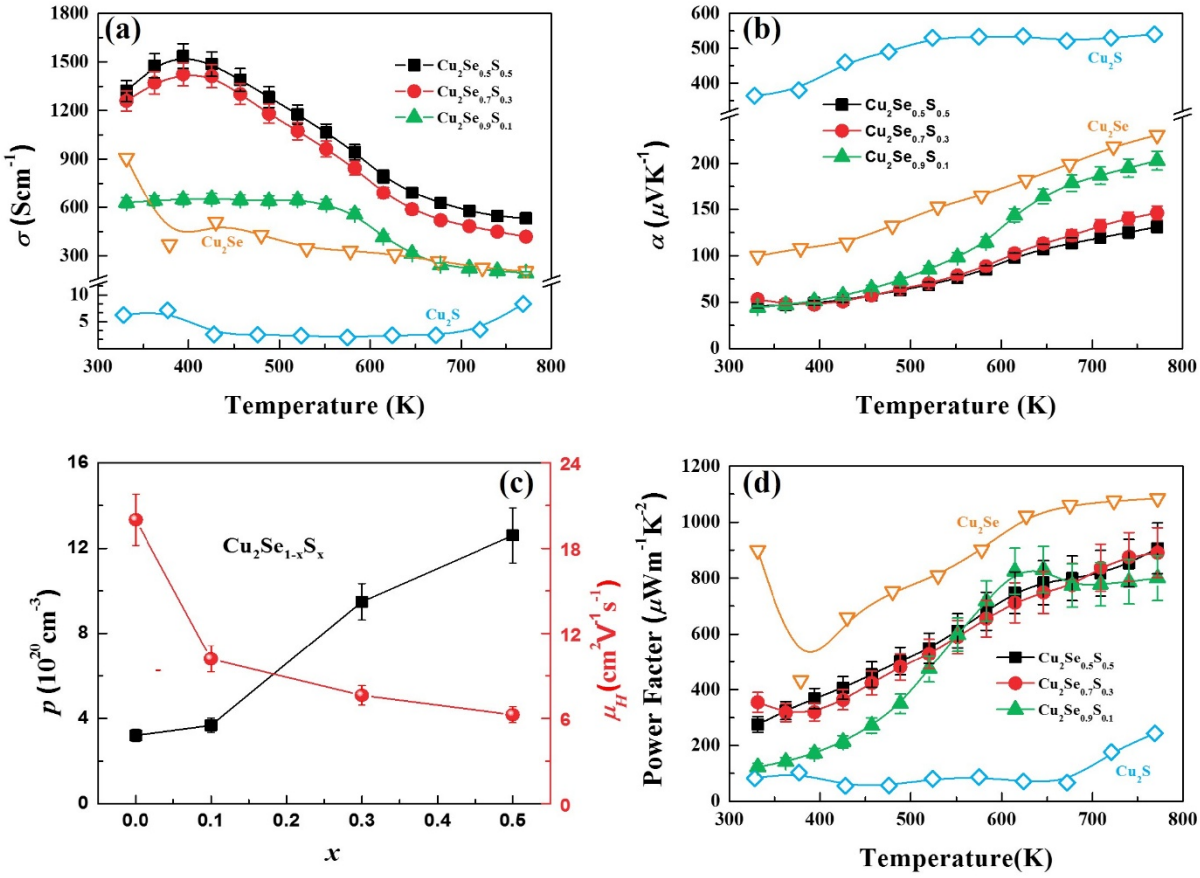

Figure 6. Temperature dependence of (a) electrical conductivity, (b) Seebeck coefficient, (d) power factor *PF* for $Cu_2Se_{1-x}S_x$ (x=0, 0.1, 0.3, 0.5 and 1).[23,36] Reproduced from ref [(36) Zhao, K. P.; Blichfeld, A. B.; Eikeland, E.; Qiu, P. F.; Ren, D. D.; Iversen, B. B.; Shi, X. and Chen, L. D. Extremely low thermal conductivity and high thermoelectric performance in liquid-like $Cu_2Se_{1-x}S_x$ polymorphic materials. *J. Mater. Chem. A*, **2017**, *5*, 18148.]. Copyright [2017] The Royal Society of Chemistry, and [(51) Yao, Y.; Zhang, B. P.; Pei, J.; Sun, Q.; Nie, G.; Zhang, W. Z.; Zhuo, Z. T.; Zhou, W. High Thermoelectric Figure of Merit Achieved in $Cu_2S_{1-x}Te_x$ Alloys Synthesized by Mechanical Alloying and Spark Plasma Sintering. *ACS Appl. Mater. Inter.* **2018**, *10*, 32201.]. Copyright [2018] American Chemical Society. (c) the carrier concentration and mobility of Cu-Se-S alloys.

The temperature dependence of the Seebeck coefficient (α) of all Cu-Se-S alloys is revealed in

Figure 6b. All the positive specimen values are acquired, demonstrating a typical *p*-type degenerate semiconductor with the main carriers of holes. The α value variation with increasing temperature was maintained after introducing S, exhibiting metallic-like behavior. α gradually decreases with increasing sulfur content, mainly caused by the increased hole concentration caused by S doping and the generated Cu vacancies. Furthermore, the nanosized precipitate of Cu_2S is generated in the matrix Cu_2Se material; thus, the introduced grain boundaries could be regarded as the scattering factor for the carrier and are beneficial for maintaining the Seebeck coefficient. This effect diminishes with rising S content since the larger size impurity generated in the material affects scattering low energy carriers less.[48] With the effects between several factors, the $Cu_2Se_{0.9}S_{0.1}$ bulk specimen possesses the highest α value of 203 μVK^{-1} at 773 K, close to that of pristine Cu_2Se at the same temperature (~220 μVK^{-1}). The power factor (*PF*) is computed by the equation $PF=\alpha^2\sigma$ shown in Figure 6d. The *PF* value of the $Cu_2Se_{0.9}S_{0.1}$ bulk specimen reaches 800 $\mu Wm^{-1}K^{-2}$ at 773 K, and the $Cu_2Se_{0.5}S_{0.5}$ specimen reaches 906 $\mu Wm^{-1}K^{-2}$ at the same temperature, confirming the Cu_2S synthesis process with high electrical performance is worthy of promotion in the preparation of ternary Cu-Se-S alloy materials. It allows the electrical transport properties of the materials to be maintained at high levels.

The Cu_2Se material has an intrinsically low thermal conductivity due to the migration of liquid-like Cu ions. The weakly bonded fluid ions could freely jump between the neighboring equilibrium positions, causing phonon scattering enhancement and transverse wave propagation inhibition.[49,50] The heat capacity, thermal diffusivity, and density for the $Cu_2Se_{1-x}S_x$ (x=0.1, 0.3, 0.5) bulk specimens are shown in Figure S5, Figure S6 and Figure S7, respectively. And the thermal conductivity (κ) of the S-alloyed Cu_2Se specimens (Figure 7) is lower than the pure specimen, especially at high temperatures. The total κ could be commonly divided into the carrier thermal conductivity (κ_e) and the lattice

thermal conductivity (κ_L) (Figure 7b-c), contributed by electrical transportation and lattice vibrations, respectively. The κ_e values are calculated by using $\kappa_e = L\sigma T$, where L is the Lorenz number with a value of 1.5×10^{-8} V^2K^{-2} in this study.[49,50] According to the electrical conductivity results shown above, introducing S into Cu_2Se improves the electrical conductivity by increasing the carrier concentration, contributing more to the thermal conductivity. Hence, κ_e dramatically rises with increasing S content, while the $Cu_2Se_{0.9}S_{0.1}$ sample still possesses a low κ_e value due to the approximated electrical conductivity. For κ_L, alloying S at Se sites results in a lattice mismatch, benefitting from stronger short-wavelength phonons at high temperatures. Moreover, the Cu_2S phase separates in situ during the synthesis process, and the introduced extra nanosized interfaces were also capable of scattering phonons. In this scenario, the κ_L of all S-alloyed specimens dramatically decreases, and the $Cu_2Se_{0.9}S_{0.1}$ bulk specimen reaches an ultralow κ value of 0.43 WmK^{-1} at 773 K.

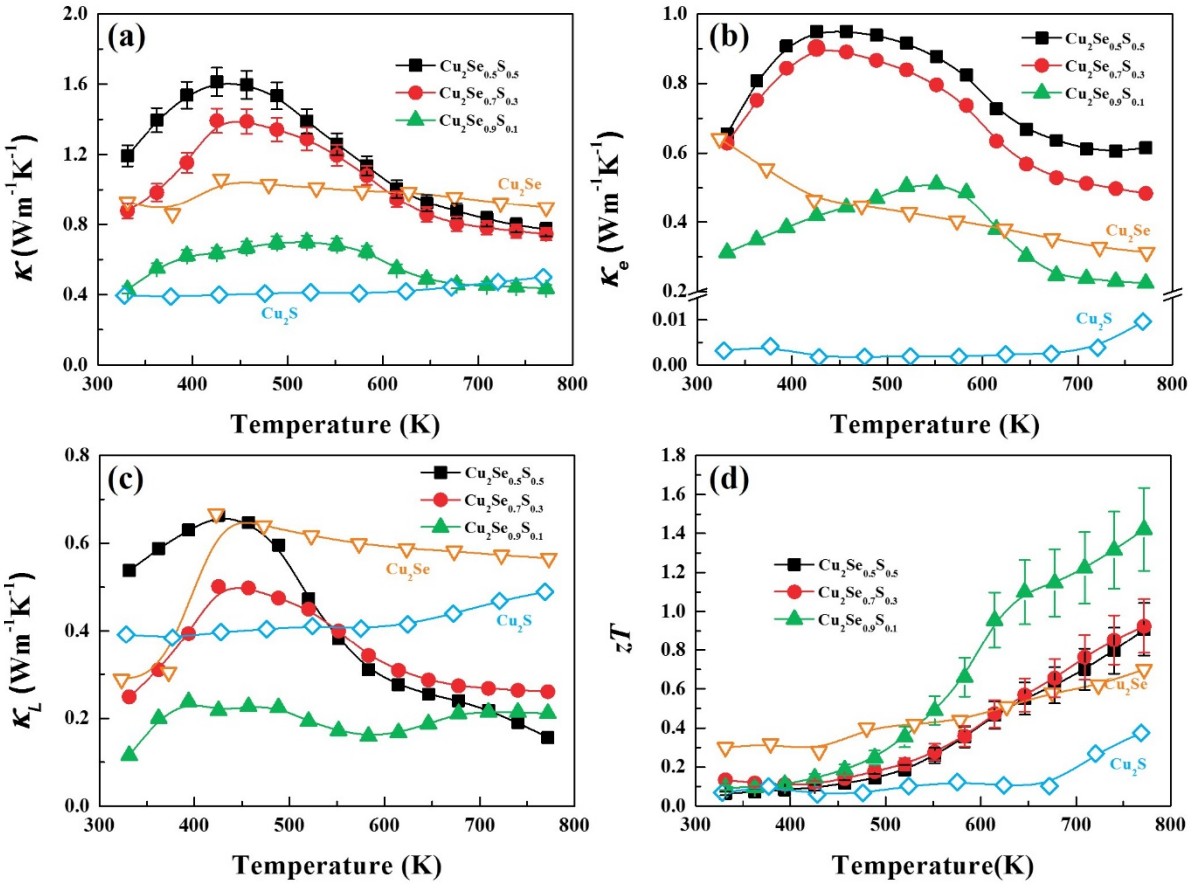

Figure 7. Temperature dependence of (a) thermal conductivity, (b) carrier thermal conductivity, (c) lattice thermal conductivity, (d) TE Figure of merit zT for $Cu_2Se_{1-x}S_x$ (x=0.1, 0.3 and 0.5) in room temperature.[36,51] Reproduced from ref 36. Copyright 2017 The Royal Society of Chemistry.

Finally, the zT value could be obtained based on the above results and is exhibited in Figure 7 d. Benefiting from the substantial drop in the thermal conductivity and the sustained electrical performance via in situ phase separation and regulating carrier concentration; the maximum zT value of 1.43 at 773 K is realized ($Cu_2Se_{0.9}S_{0.1}$ bulk specimen), which is 101.4% higher than pure Cu_2Se (zT=0.71 @ 773 K) and 286.5% higher than pure Cu_2S (zT=0.37 @ 773 K). This work proposes a new strategy for optimizing the TE properties of Cu-Se-S alloys by in situ phase separation technology, which could be an efficient route for improving the TE properties of other ternary or multielement alloy materials.

CONCLUSION

Based on a similar synthesis method utilized in Cu_2S materials with ultrahigh electrical conductivity, the thermoelectric performance of Cu_2Se-based materials was significantly enhanced via in situ phase separation technology. The phenomenon of Cu_2S nanocrystals embedded throughout the Cu_2Se matrix was detected in the Cu-Se-S alloy system for the first time. The Cu_2S phase spontaneously precipitated from the matrix during the sintering process instead of generating a commonly uniform alloy. Contrary to the Cu-Se-S system previously reported, expressing a different type of nanostructure with a uniform matrix and no precipitate. Such a spontaneous phase separation process negatively affects the electrical performance of the material but enhances the phonon scattering. As a result, large-scale $Cu_2Se_{1-x}S_x$ (x=0.1, 0.3, and 0.5) nanocrystals were fabricated by the hydrothermal synthesis method. The SPS-treated $Cu_2Se_{0.9}S_{0.1}$ bulk sample acquired a zT value of 1.43

at 773 K, which is currently the optimum reported value for the $Cu_2Se_{1-x}S_x$ system at this temperature. Nanoparticles formed by spontaneous phase separation are vital for decreasing thermal conductivity, and extensions of this in situ phase separation approach may be suitable in other TE materials.

ASSOCIATED CONTENT

Supporting Information

The Supporting Information is available free of charge at xxxxxxxx.

Energy dispersive spectrometer (EDS) images and the specific content of Cu, Se, S elements for (a) $Cu_2Se_{0.5}S_{0.5}$, (b) $Cu_2Se_{0.7}S_{0.3}$ and (c) $Cu_2Se_{0.9}S_{0.1}$ powders (Figure S1); Rietveld refinement patterns of Cu-Se-S powders and the bulk specimens (Figure S2); Lattice parameters of $Cu_2Se_{1-x}S_x$ by the XRD data (Figure S3); EPMA elemental mapping of the (a) $Cu_2Se_{0.5}S_{0.5}$ and (b) $Cu_2Se_{0.7}S_{0.3}$ bulk specimens (Figure S4); The heat capacity for the $Cu_2Se_{1-x}S_x$ (x=0.1, 0.3, 0.5) bulk specimens calculated by the Neumann-Kopp rule during 323 K to 773 K (Figure S5); Temperature dependence of thermal diffusivity of the $Cu_2Se_{1-x}S_x$ (x=0.1, 0.3, 0.5) bulk specimens (Figure S6); The mass density of the $Cu_2Se_{1-x}S_x$ (x=0.1, 0.3, 0.5) bulk specimens (Figure S7).

AUTHOR INFORMATION

Corresponding Authors

Zhenhua Ge - *Faculty of Materials Science and Engineering, Kunming University of Science and Technology, Kunming 650093, P.R. China*

Email: zge@kust.edu.cn

Jing Feng - *Faculty of Materials Science and Engineering, Kunming University of Science and Technology, Kunming 650093, P.R. China*

Email: vdmzsfj@qq.com

Authors

Yixin Zhang - *Faculty of Materials Science and Engineering, Kunming University of Science and Technology, Kunming 650093, P.R. China;* orcid.org/0000-0002-8456-7674

Yunqiao Tang - *Faculty of Materials Science and Engineering, Kunming University of Science and Technology, Kunming 650093, P.R. China*

Zheng Ma - *Ernst Ruska-Centre for Microscopy and Spectroscopy with Electrons and Peter Grünberg Institute, Forschungszentrum Jülich, 52425, Jülich, Germany.*

Mingyu Hu - *School of Chemical Biology and Biotechnology, Shenzhen Graduate School, Peking University, Shenzhen 518055, China*

Jing Feng - *Faculty of Materials Science and Engineering, Kunming University of Science and Technology, Kunming 650093, P.R. China*

Notes

The authors declare no competing financial interest.

ACKNOWLEDGEMENTD

This work was supported by the National Natural Science Foundation of China (Grant No. 51501086 and 11764025) and the Academician (Expert) Workstation of Yunnan Province Program (Grant No.202005AF150010).

REFERENCES

(1) Sootsman, J. R.; Chung, D. Y.; Kanatzidis, M. G.; New and old concepts in thermoelectric materials. *Angew. Chem. Int. Edit.* **2009**, *48*, 8616-8639.

(2) Sales, B. C.; Smaller is cooler. *Science* **2002**, *295*, 1248-1249.

(3) DiSalvo, F. J. Thermoelectric Cooling and Power Generation. *Science* **1999**, *285*, 703-706.

(4) Poudel, B.; Hao, Q.; Ma, Y.; Lan, Y. C.; Minnich, A.; Yu, B.; Yan, X.; Wang, D. Z.; Muto, A.; Vashaee, D.; Chen, X.; Liu, J.; Dresselhaus, M. S.; Chen, G.; Ren, Z. F. High-thermoelectric performance of nanostructured bismuth antimony telluride bulk alloys. *Science* **2008**, *320*, 634-638.

(5) Snyder, G. J.; Eric, S. T. Complex thermoelectric materials. *Nat. Mater.* **2008**, *7*, 105-114.

(6) Zeier, W. G.; Zevalkink, A.; Gibbs, Z. M.; Hautier, G.; Kanatzidis, M. G.; Snyder, G. J. Thinking like a chemist: intuition in thermoelectric materials. *Angew. Chem. Int. Ed.* **2016**, *55*, 6826-6841.

(7) Heremans, J. P.; Jovovic, V.; Toberer, E. S.; Saramat, A.; Kurosaki, K.; Charoenphakdee, A.; Yamanaka, S.; Snyder, G. J. Enhancement of thermoelectric efficiency in PbTe by distortion of the electronic density of states. *Science* **2008**, *321*, 554-557.

(8) Kim, S. I.; Lee, K. H.; Mun, H. A.; Kim, H. S.; Hwang, S. W.; Roh, J. W.; Yang, D. J.; Shin, W. H.; Li, X. S.; Lee, Y. H. Dense dislocation arrays embedded in grain boundaries for high-performance bulk thermoelectric. *Science* **2015**, *348*, 109-114.

(9) Zebarjadi, M.; Esfarjani, K.; Dresselhaus, M.; Ren, Z.; Chen, G. Perspectives on thermoelectrics: from fundamentals to device applications. *Energy Environ. Sci.* **2012**, *5*, 5147-5162.

(10) Shi, X.; Chen, L. Thermoelectric materials step up. *Nat. Mater.* **2016**, *15*, 691-692.

(11) Harman, T. C.; Taylor, P. J.; Walsh, M. P.; LaForge, B. E. Quantum dot superlattice thermoelectric materials and devices. *Science* **2002**, *297*, 2229-2232.

(12) Böttner, H.; Chen, G.; Venkatasubramanian, R. Aspects of thin-film superlattice thermoelectric materials, devices and applications. *MRS bull.* **2006**, *31*, 211-217.

(13) Nolas, G. S.; Sharp, J. W.; Goldsmid, H. J. Thermoelectrics: Basic Principles and New Materials Developments. *Springer Berlin* **2001**.

(14) Rowe, D. M. Thermoelectrics Handbook: Macro to Nano; CRC Press: Boca Raton, FL, **2006**.

(15) Minnich, A. J.; Dresselhaus, M. S.; Ren, Z. F.; Chen, G. Bulk nanostructured thermoelectric materials: current research and future prospects. *Energ. Environ. Sci.* **2009**, *2*, 466-479.

(16) Hsu, K. F.; Loo, S.; Guo, F.; Chen, W.; Dyck, J. S.; Uher, C.; Kanatzidis, M. G. Cubic $AgPb_mSbTe_{2+m}$: bulk thermoelectric materials with high figure of merit. *Science* **2004**, *303*, 818-821.

(17) Snyder, G. J.; Toberer, E. S. Complex thermoelectric materials. *Materials for Sustainable Energy: A Collection of Peer-Reviewed Research and Review Articles from Nature Publishing Group*. **2011**, 101-110.

(18) Dresselhaus, M. S.; Chen, G.; Tang, M. Y.; Yang, R. G.; Lee, H.; Wang, D. Z.; Ren, Z. F.; Fleurial, J. P.; Gogna, P. New directions for low-dimensional thermoelectric materials. *Adv. Mater.* **2007**, *19*, 1043-1053.

(19) Ge, Z. H.; Ji, Y. H.; Qiu, Y.; Chong, X. Y.; Feng, J.; He, J. Q. Enhanced thermoelectric properties of bismuth telluride bulk achieved by telluride-spilling during the spark plasma sintering process. *Scripta. Mater.* **2018**, *143*, 90-93.

(20) Zhao, L. D.; Zhang, B. P.; Liu, W. S.; Li, J. F. Effect of mixed grain sizes on thermoelectric performance of Bi_2Te_3 compound. *J. Appl. Phys.* **2009**, *105*, 023704.

(21) Lu, P. X.; Wang, X. B.; Lu, M. M. Largely enhanced thermoelectric properties of the binary-phased PbTe–Sb_2Te_3 nanocomposites. *J. Mater. Res.* **2012**, *27*, 734-739.

(22) Cao, Y. Q.; Zhu, T. J.; Zhao, X. B. Low thermal conductivity and improved figure of merit in fine-grained binary PbTe thermoelectric alloys. *J. Appl. Phys.* **2008**, *42*, 015406.

(23) Liu, H. L.; Shi, X.; Xu, F. F.; Zhang, L. L.; Zhang, W. Q.; Chen, L. D.; Uher, C.; Day, T.; Snyder,

G. J. Copper ion liquid-like thermoelectrics. *Nat. Mater.* **2012**, *11* 422-425.

(24) Xiao, X. X.; Xie, W. J.; Tang, X. F.; Zhang, Q. J. Phase transition and high temperature thermoelectric properties of copper selenide $Cu_{2-x}Se$ ($0 \leq x \leq 0.25$). *Chinese. Phys. B* **2011**, *20*, 087201.

(25) He, Y.; Day, T.; Zhang, T. S.; Liu, H. L.; Shi, X.; Chen, L. D.; Snyder, G. J. High Thermoelectric Performance in Non-Toxic Earth-Abundant Copper Sulfide. *Adv. Mater.* **2014**, *26*, 3974-3978.

(26) Ge, Z. H.; Zhao, L. D.; Wu, D.; Zhang, B. P.; Li, J. F.; He, J. Q. Low cost, abundant binary sulfides as promising thermoelectric. *Mater. Today* **2016**, *19*, 227-239.

(27) Zhao, Y. X.; Pan, H. C.; Lou, Y. B.; Qiu, X. F.; Zhu, J. J.; Burda, C. Plasmonic $Cu_{2-x}S$ nanocrystals: optical and structural properties of copper-deficient copper (I) sulfides. *J. Am. Chem. Soc.* **2009**, *131*, 4253–4261.

(28) Rivest, J. B.; Fong, L. K.; Jain, P. K.; Toney, M. F.; Alivisatos, A. P. Size dependence of a temperature-induced solid–solid phase transition in copper (I) sulfide. *J. Phys. Chem. Lett.* **2011**, *2*, 2402-2406.

(29) Kang, S. D.; Danilkin, S. A.; Aydemir, U.; Avdeev, M.; Studer A. and Snyder, G. J. Apparent critical phenomena in the superionic phase transition of $Cu_{2-x}Se$. *New J. Phys.*, **2016**, *18*, 013024.

(30) He, Y.; Lu, P.; Shi, X.; Xu, F.; Zhang, T.; Snyder, G. J.; Uher C. and Chen, L. Ultrahigh thermoelectric performance in mosaic crystals. *Adv. Mater.*, **2015**, *27*, 3639-3644.

(31) Zhao, K. P.; Guan, M. J.; Qiu, P. F.; Blichfeld, A. B.; Eikeland, E.; Zhu, C. X.; Ren, D. D.; Xu, F. F.; Iversen, B. B.; Shi X. and Chen, L. D. Thermoelectric properties of $Cu_2Se_{1x}Te_x$ solid solutions. *J. Mater. Chem. A*, **2018**, *6*, 6977.

(32) Zhao, K. P.; Qiu, P. F.; Song, Q. F.; Blichfeld, A. B.; Eikeland, E.; Ren, D. D.; Ge, B. H.; Iversen, B. B.; Shi, X.; Chen, L. D. Ultrahigh thermoelectric performance in $Cu_{2-y}Se_{0.5}S_{0.5}$ liquid-like

materials. *Mater. Today. Phys.* **2017**, *1*, 14-23.

(33) Zhao, K. P.; Blichfeld, A. B.; Chen, H. Y.; Song, Q. F.; Zhang, T. S.; Zhu, C. X.; Rem, D. D.; Hanus, R.; Qiu, P. F.; Iversen, B. B.; Xu, F. F.; Snyder, G. J.; Shi, X. and Chen, L. D. Enhanced Thermoelectric Performance through Tuning Bonding Energy in $Cu_2Se_{1-x}S_x$ Liquid-like Materials. *Chem. Mater.*, **2017**, *29*, 6367.

(34) Yao, Y.; Zhang, B. P.; Pei, J.; Liu Y.C. and Li, J. F. Thermoelectric performance enhancement of Cu_2S by Se doping leading to a simultaneous power factor increase and thermal conductivity reduction. *J. Mater. Chem. C*, **2017**, *5*, 7845.

(35) Farooq, M. U.; Butt, S.; Gao, K. W.; Sun, X. G.; Pang, X. L.; Khan, S. U.; Xu, W. Mohmed, F.; Mahmood, A.; Mahmood, N. Enhanced Thermoelectric Efficiency of $Cu_{2-x}Se$-Cu_2S Composite by Incorporating Cu_2S Nanoparticles. *Ceram. Int.*, **2016**, *42*, 8395-8401.

(36) Zhao, K. P.; Blichfeld, A. B.; Eikeland, E.; Qiu, P. F.; Ren, D. D.; Iversen, B. B.; Shi, X. and Chen, L. D. Extremely low thermal conductivity and high thermoelectric performance in liquid-like $Cu_2Se_{1-x}S_x$ polymorphic materials. *J. Mater. Chem. A*, **2017**, *5*, 18148.

(37) Tang, Y. Q.; Ge, Z. H.; Feng, J. Synthesis and Thermoelectric Properties of Copper Sulfides via Solution Phase Methods and Spark Plasma Sintering. *Crystals* **2017**, *7*, 141.

(38) Liu, W. D.; Shi, X. L.; Hong, M.; Yang, L.; Moshwan, R.; Chen Z. G.; Zou, J. Ag doping induced abnormal lattice thermal conductivity in Cu_2Se. *J. Mater. Chem. C* **2018**, *6*, 13225.

(39) Mao, T.; Qiu, P. F.; Du, X. L.; Hu, P.; Zhao, K. P.; Xiao, J.; Shi, X.; Chen, L. D. Enhanced Thermoelectric Performance and Service Stability of Cu_2Se Via Tailoring Chemical Compositions at Multiple Atomic Positions. *Adv. Func. Mater.* **2019**, 1908315.

(40) Zhu, Y. B.; Zhang B. P.; Liu, Y. Enhancing thermoelectric performance of Cu_2Se by doping Te, *Phys. Chem. Chem. Phys.* **2017**, *19*, 27664.

(41) Kong, F. F.; Bai, J.; Zhao, Y. W.; Liu, Y.; Shi, J.; Wang, Z. Y.; Xiong, R. Ultralow thermal conductivity and high thermoelectric performance of Cu_2Se/TiO_2 nanocomposite. *Appl. Phys. Lett.* **2019**, *115*, 203901

(42) Yu, J. L.; Zhao, K. P.; Qiu, P. F.; Shi, X.; Chen, L. D. Thermoelectric properties of copper-deficient $Cu_{2-x}Se$ ($0.05 \leqslant x \leqslant 0.25$) binary compounds. *Ceram. Int.* **2017**, *43*, 11142-11148.

(43) Kong, F. F.; Bai, J.; Bi, P.; Liu, X. W.; Wang, Z. Y.; Xiong, R. *Ceram. Int.* **2019**, *45*, 8866-8872.

(44) Miyatani, S. Y.; Mori, S.; Yanagihara, M. Phase diagram and electrical properties of $Cu_{2-\delta}Te$. *J. Phys. Soc. Jpn.* **1979**, *47*, 1152-1158.

(45) Tang, Y. Q.; Ge, Z. H.; Chen, Y. X.; Qin, P.; Feng, J.; He, J. Q. Thermoelectric properties of Cu_2Se_x prepared by solution phase methods and spark plasma sintering. *J. Eur. Ceram. Soc.* **2017**, *37*, 4687-4692.

(46) Riha, S. C.; Johnson, D. C.; Prieto, A. L. Cu_2Se nanoparticles with tunable electronic properties due to a controlled solid-state phase transition driven by copper oxidation and cationic conduction. *J. Am. Chem. Soc.* **2010**, *133*, 1383-1390.

(47) Zhu, W. M.; Huang, Z. Y.; Chu, M. H.; Li, S. K.; Zhang, Y. H.; Ao, W. Q.; Wang, R.; Luo, J.; Liu, F. S.; Xiao, Y. G.; Pan, F. Enhanced thermoelectric performance through optimizing structure of anionic framework in AgCuTe-based materials. *Chem. Eng. J.* **2020**, *386*, 123917.

(48) Faleev, S. V.; Leonard, F. Theory of enhancement of thermoelectric properties of materials with nanoinclusions. *Phys. Rev. B* **2008**, *77*, 214304.

(49) Qiu, P. F.; Shi, X.; Chen, L. D. Cu-based thermoelectric materials. *Energy Storage Mater.* **2016**, *3*, 85-97.

(50) Zhao, K. P.; Qiu, P. F.; Shi, X.; Chen, L. D. Recent Advances in Liquid-Like Thermoelectric Materials. *Adv. Func. Mater.* **2020**, *30*, 1903867.

(51) Yao, Y.; Zhang, B. P.; Pei, J.; Sun, Q.; Nie, G.; Zhang, W. Z.; Zhuo, Z. T.; Zhou, W. High Thermoelectric Figure of Merit Achieved in $Cu_2S_{1-x}Te_x$ Alloys Synthesized by Mechanical

Alloying and Spark Plasma Sintering. *ACS Appl. Mater. Inter.* **2018**, *10*, 32201.

For Table of Contents Only

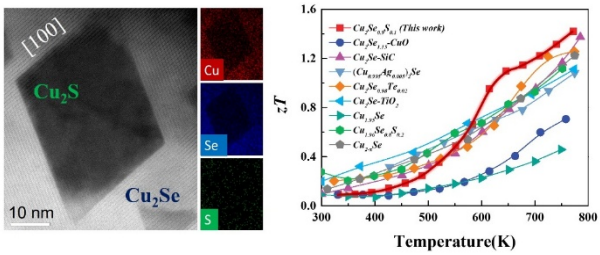

Benefiting from the maintained electrical transport properties and the obviously reduced thermal conductivity by generating the complex microstructure, $Cu_2Se_{0.9}S_{0.1}$ bulk sample finally achieves the maximum *zT* value of 1.43 at 773 K, which is currently the highest reported value for the $Cu_2Se_{1-x}S_x$ system at this temperature.